

Photoacoustic Analysis of Matrix-Assisted Laser Desorption/Ionization Processes with Pulsed Infrared Lasers

Andreas Rohlffing,[†] Christoph Menzel,[†] Lalit M. Kukreja,[‡] Franz Hillenkamp,[†] and Klaus Dreisewerd^{*,†}

Institute of Medical Physics and Biophysics, University of Münster, Robert-Koch-Str. 31, D-48149 Münster, Germany, and Thin Film Laboratory, Centre for Advanced Technology, P.O. CAT, Indore – 452 013, India

Received: June 3, 2003; In Final Form: August 20, 2003

A fast piezoelectric detection system was utilized to record time-resolved photoacoustic signals reflecting the thermal expansion and the rate of material ablation in infrared matrix-assisted laser desorption/ionization (IR-MALDI). Glycerol was employed as a liquid and 2,5-dihydroxybenzoic acid (2,5-DHB) as a crystalline matrix. An Er:YAG laser ($\lambda = 2.94\ \mu\text{m}$; $\tau_L \sim 100\ \text{ns}$) and a wavelength-tunable optical parametric oscillator (OPO) laser system ($\lambda = 1.4\text{--}4.0\ \mu\text{m}$; $\tau_L = 6\ \text{ns}$) were used for desorption/ionization. Material ejection and MALDI ion signals were recorded as a function of laser fluence, pulse duration, and wavelength. For glycerol as matrix, material ejection was found to be temporally confined to about the laser pulse duration when the OPO was employed. For excitation with the Er:YAG laser, a prolonged material ejection with an approximately exponential decay was observed with a characteristic time constant of $\sim 1\ \mu\text{s}$. For both lasers, material ejection was observed already at fluences substantially below the MALDI ion threshold. For excitation with the OPO, a correlation between a change in the desorption/ablation mechanism and the onset of ion generation was found. Crystalline 2,5-DHB preparations were investigated with the OPO only. Material ejection from this matrix was found to exhibit a significantly different dependence of the overall ejected material on laser fluence. The article also provides an introduction to the underlying photoacoustic theory adapted to the MALDI process.

Introduction

Over recent years, matrix-assisted laser desorption/ionization mass spectrometry (MALDI-MS^{1,2}) has emerged as an established technique for the analysis of a wide range of biomolecular compounds. Lasers emitting in the ultraviolet (UV)^{2,3} or infrared (IR) wavelength range^{4–9} are employed for MALDI-MS. Although, for sensitivity and several other technical reasons, the use of UV lasers is much more common than that of IR lasers, IR-MALDI has been found to be the method of choice in several specific applications, for example, in the analysis of particularly large and/or labile analyte compounds.^{10,11}

The mechanisms underlying UV- and IR-MALDI have been reviewed in refs 9 and 12. Most fundamental studies relied on the MALDI ion signals, recorded, for example, as a function of the irradiation parameters. However, this approach fails to account for the strong convolution of material disintegration and ionization. Also, when the ions are studied, only a minor fraction of the overall ejected material plume is probed.¹³ Moreover, comparative UV-/IR-MALDI studies show that thermodynamically controlled secondary ionization reactions in the MALDI plume mask entirely different entrance-channel characteristics arising from electron versus vibrational excitation mechanisms, respectively.^{9,14,15} Even post-ionization of individual molecules and possibly clusters in the MALDI plume^{12,16–20} yields only partial information on the overall

desorption/ablation mechanism. Especially in IR-MALDI, where penetration depths on the order of several micrometers are typical, a wide cluster-size distribution must be expected, and a simpler approach correlating ionization and total ablation yields would seem to be very helpful.

The present article describes experiments that are based on the analysis of photoacoustic (PA) stress wave signals induced by the laser–material interaction. A mathematical treatment allows to extract the ejection-related recoil component straightforwardly from the overall PA signal, which is dominated by the thermoelastic response. Sensitive PA stress wave analysis has been reported before for the laser ablation of polymers^{21,22} and for medical laser applications,^{23–26} however, without extracting the ablation-related component. Moreover, in these studies, an open-circuit detection scheme was realized, in contrast to the approximated “short-circuit” mode realized in the present study. The consequences of these differences are outlined in the Experimental Section.

Because of the low penetration depths of UV laser radiation into the matrix of 50–200 nm, only very small amounts of material are ejected under common UV-MALDI conditions.²⁷ Consequently, a weak ablation-related compressive stress signal is generated. The photoacoustic detection of material ejection in UV-MALDI is, therefore, very challenging. For IR-MALDI, laser penetration depths are higher by at least 1 order of magnitude, and correspondingly larger amounts of material are ablated per laser pulse. Both effects enhance photoacoustic signal generation considerably. The present work, therefore, focuses on IR-MALDI and, moreover, on that with glycerol as liquid IR matrix. Due to its liquid state, glycerol provides an

* To whom correspondence should be addressed. E-mail. dreisew@uni-muenster.de.

[†] University of Münster.

[‡] Centre for Advanced Technology.

intrinsically homogeneous sample morphology which significantly promotes an undisturbed propagation of stress waves. Some results for crystalline 2,5-dihydroxybenzoic acid (2,5-DHB) preparations are also presented.

Two different IR lasers with pulse durations of 6 and 100 ns were employed. For glycerol as matrix, this comparison reveals a substantial influence of the laser pulse duration on the time course of the material disintegration process. The dependence of the overall amount of ablated material on the laser fluence is also presented and compared to predictions derived from theoretical MALDI desorption/ablation models and to the ion signal intensity as a function of fluence. To a certain extent, this allows us to draw conclusions on the physical mechanisms of laser-induced ablation as well as on a possible correlation between the ablation and the ionization mechanism.

Theory of Photoacoustic Signal Generation

Pulsed laser irradiation of an absorbing sample results in the generation of photoacoustic stress waves induced by rapid heating and the subsequent build-up of compressive stress, which is, in the case of a free surface, followed by a rapid expansion. If this process is reversible (no ablation, photochemical reactions, etc.), then the resulting stress waves are referred to as “thermoelastic”. The initially purely compressive stress splits into two stress wave components, one propagating into the bulk of the sample and the other propagating outward. The outward-propagating component is reflected at the free surface with a phase reversal, leading to the formation of a tensile component of equal amplitude and duration. This tensile component travels into the sample, trailing the original compressive component; consequently, the overall thermoelastic stress wave is a bipolar compression/tension wave.

Ablation leads to the generation of an additional, purely compressive component caused by the recoil momentum of the ablated material affecting the remaining sample. Although thermoelastic and ablation-induced stress wave generation may influence one another, both mechanisms will be treated separately in this article as a first-order approximation.

Thermoelastic Stress Waves. A basic theoretical treatment of thermoelastic stress wave generation has been given in an early article by Gournay.²⁸ On the basis of a one-dimensional linear hydrodynamic model and assuming an excitation by a temporally rectangular laser pulse of duration T as well as free boundary conditions at the homogeneously irradiated sample surface of infinite extent, his model yields the thermoelastic stress σ as

$$\sigma(\tau) = \frac{c\beta I}{2C_V} \cdot \begin{cases} (1 - e^{-\alpha c T}) \cdot e^{\alpha c \tau}, & \tau < 0 \\ e^{-\alpha c \tau} - e^{\alpha c(\tau-T)}, & 0 < \tau < T \quad (t > 0) \\ (1 - e^{-\alpha c T}) \cdot e^{-\alpha c \tau}, & \tau > T \end{cases} \quad (1)$$

where $\tau = t - z/c$ is the reduced time (i.e., time t measured from the onset of the excitation pulse minus the propagation time of the stress wave from the surface to the sample depth z), c is the velocity of sound, β is the thermal expansion coefficient, I is the irradiance (pulse energy per pulse duration T and unit area of the incident laser radiation), C_V is the specific heat at constant volume, and α is the optical absorption coefficient of the sample at the employed laser wavelength. Equation 1 is valid only for a sample depth z much greater than the optical penetration depth α^{-1} (i.e., for $\alpha \cdot z \gg 1$).

Gournay had confined his treatment to rectangular excitation pulses. For a temporally Gaussian pulse shape, more typical of

real experimental conditions, the resulting thermoelastic stress can be deduced by means of linear response theory by solving the convolution integral

$$\sigma_{Th}(\tau) = I(t) \otimes \sigma_\delta(\tau) \quad (2)$$

where $\sigma_{Th}(\tau)$ is the resulting thermoelastic stress wave after excitation with a laser pulse of temporal profile $I(t)$. $\sigma_\delta(\tau)$ is the system response function, i.e., the solution of the underlying differential wave equation for an infinitesimally short (Dirac δ function) pulse. $\sigma_\delta(\tau)$ can be calculated from eq 1 by taking the limit for $T \rightarrow 0$ with $I \propto 1/T$, which yields

$$\sigma_\delta(\tau) = \frac{\alpha c^2 \beta}{2C_V} \cdot \begin{cases} e^{\alpha c \tau}, & \tau < 0 \\ -e^{-\alpha c \tau}, & \tau > 0 \end{cases} \quad (3)$$

With the Gaussian laser profile

$$I_G(t') = I_0 \cdot \exp\left(-\frac{4 \ln 2 \cdot t'^2}{\tau_L^2}\right) \quad (4)$$

where I_0 is the peak intensity at $t' = 0$ and τ_L is the fwhm of the Gaussian profile, the convolution of the Gaussian pulse with the response function yields the thermoelastic stress wave σ_{Th} as

$$\sigma_{Th}(\tau) = K \cdot [e^{\alpha c \tau} \cdot \operatorname{erfc}(x_0 + x_\tau \cdot \tau) - e^{-\alpha c \tau} \cdot \operatorname{erfc}(x_0 - x_\tau \cdot \tau)] \quad (5)$$

with

$$K = \frac{\alpha c^2 \beta}{2C_V} \cdot \frac{H}{2} \cdot \exp\left(\frac{\alpha^2 c^2 \tau_L^2}{16 \ln 2}\right) \quad x_0 = \frac{\alpha c \tau_L}{4\sqrt{\ln 2}} \quad x_\tau = \frac{2\sqrt{\ln 2}}{\tau_L}$$

and the total fluence H (i.e., the energy incident per unit area).

Equation 5 reveals two important features: (A) for constant values of the absorption coefficient α and the laser pulse duration τ_L , the amplitude of a thermoelastic stress wave is proportional to the total fluence H of the incident radiation and (B) a strict point-symmetry

$$\sigma_{Th}(-\tau) = -\sigma_{Th}(\tau) \quad (6)$$

holds.

In addition to its dependence on laser fluence, the amplitude of a thermoelastic stress wave depends strongly on the ratio of the laser pulse duration, τ_L , to the transit time, τ_{ac} , of the stress wave through the excitation volume, commonly estimated by $\alpha^{-1}c^{-1}$. For $\tau_L \ll \tau_{ac}$, the stress wave remains essentially inside the excitation volume during the entire laser pulse. Hence, the deposited radiant energy contributes very efficiently to the build-up of eventually extremely high stress amplitudes. The inequality $\tau_L \ll \alpha^{-1}c^{-1}$ is, therefore, often referred to as the “acoustic” or “stress confinement” condition. In contrast, for a pulse duration much longer than the transit time ($\tau_L \gg \tau_{ac}$), a part of the thermoelastic stress leaves the excitation volume while radiant energy is still being deposited. Hence, the amplitude of the stress wave is correspondingly smaller.

Ablation-Induced Stress Waves. In the following one-dimensional treatment, ejection is assumed to take place homogeneously over an infinitely extended surface and exclusively perpendicular to the sample surface. In this case, ablation

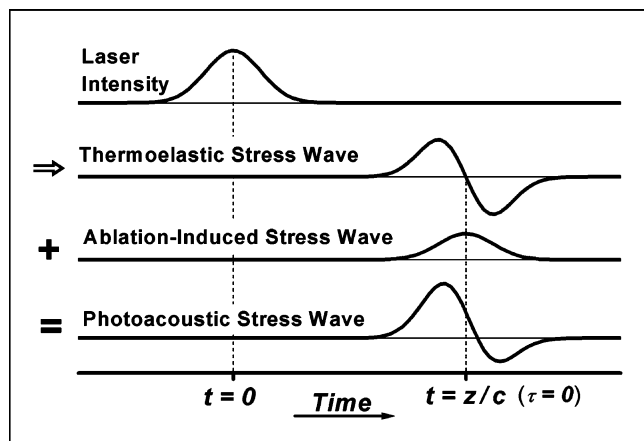


Figure 1. Schematic representation of the superposition of bipolar thermoelastic and purely compressive ablation-induced stress wave components yielding the overall laser-induced photoacoustic stress transient accessible by acoustic measurements. The delay of z/c between the peak laser intensity and the zero crossing of the thermoelastic stress wave corresponds to the propagation time of the stress wave from the sample surface to the detector plane. (c is the velocity of sound.)

had to be described, in principle, by a differential value such as “mass per area”. However, for the sake of clarity, a finite ablated mass will be considered in the following model, yielding essentially the same results.

Each ejected particle has an individual forward velocity v that may be altered during expansion by collisions, and the overall ejection plume is characterized by a (time-dependent) velocity distribution $f(v) dv$. In the following, the average ejection velocity, \bar{v} , is assumed to remain unaltered throughout the entire ablation process and to be independent of laser fluence to a first-order approximation.²⁹ Let $dm(t)$ then be the mass of material that is ejected during an infinitesimal time interval from t to $t + dt$. Within dt , the total forward momentum $dP(t) = \bar{v} dm(t)$ is transferred to the ejected mass, which implies that an accelerating force

$$F(t) = \frac{dP(t)}{dt} = \bar{v} \cdot \frac{dm(t)}{dt} = \bar{v} \cdot \dot{m}(t) \quad (7)$$

must act on the ablated material, where $\dot{m}(t)$ represents the momentary rate of material ejection. Consequently, an equally strong recoil force acts on the remaining sample surface A and induces a purely compressive stress

$$\sigma_{\text{Abl}}(t) = \frac{F(t)}{A} = \frac{\bar{v}}{A} \cdot \dot{m}(t) \geq 0 \quad (8)$$

This ablation-induced stress at the sample surface gives rise to the formation of a compressive stress wave

$$\sigma_{\text{Abl}}(\tau) = \frac{\bar{v}}{A} \cdot \dot{m}(\tau) \quad \tau = t - \frac{z}{c} \quad (9)$$

propagating into the sample. Hence, the overall photoacoustic signal σ_{PA} is a superposition of both the thermoelastic and the ablation-related wave:

$$\sigma_{\text{PA}}(\tau) = \sigma_{\text{Th}}(\tau) + \sigma_{\text{Abl}}(\tau) \quad (10)$$

Figure 1 shows schematically this superposition of the thermoelastic and compressive ablation-induced pressure waves. The thermoelastic signal is symmetric about the zero of amplitude, whereas the ablation-induced wave is always positive and thus can break the symmetry of the overall stress wave signal.

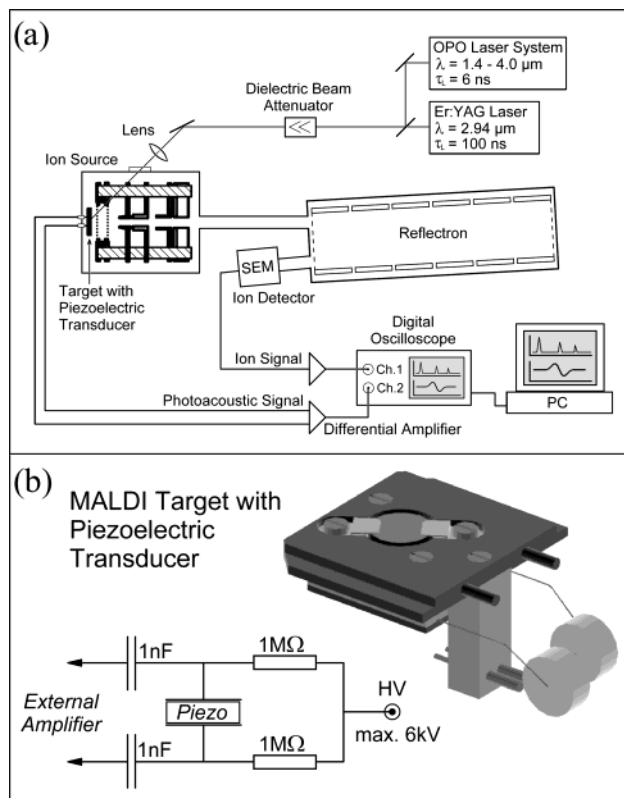


Figure 2. Experimental setup for simultaneous recording of laser-induced photoacoustic stress transients and MALDI ion signals. (a) The employed reflectron-TOF mass spectrometer with the two different IR desorption lasers. Ion signals are detected with a secondary electron multiplier and recorded with the first channel of a digital oscilloscope. (b) A piezoelectric transducer disk of 5 mm thickness and 10 mm diameter, mounted high-voltage proof into a standard MALDI sample plate, was used for the time-resolved detection of laser-induced photoacoustic stress waves. Samples were prepared directly on the transducer surface. Signals were amplified by an external differential amplifier and recorded with the second channel of the digital oscilloscope.

The symmetry of the thermoelastic component proves to be helpful for a rather facile determination of the overall material ablation from photoacoustic measurements because, as a consequence, the time integral of the thermoelastic component, σ_{Th} , strictly equals zero:

$$\int \sigma_{\text{Th}}(\tau) d\tau \equiv 0 \quad (11)$$

Hence, a simple time integration of the overall photoacoustic signal yields

$$\int \sigma_{\text{PA}}(\tau) d\tau = \int \sigma_{\text{Abl}}(\tau) d\tau = \frac{\bar{v}}{A} \cdot m(t \rightarrow \infty) = \frac{\bar{v}}{A} \cdot m_{\text{total}} \quad (12)$$

and therefore a measure of the overall ablated mass per single laser pulse, m_{total} .

Experimental Section

Time-of-Flight Mass Spectrometer. All experiments were carried out with an in-house-built single-stage reflectron time-of-flight mass spectrometer (TOF-MS) of 3.5 m equivalent drift length (Figure 2a). The back pressure in the mass spectrometer was $\sim 2 \times 10^{-6}$ mbar. Samples were observed with a CCD camera. A two-stage Wiley/McLaren-type ion extraction source

with planar grids at distances from the target of 6 and 18.5 mm was employed for ion acceleration. Experiments were performed using static ion extraction with a target voltage of 6 kV and the first grid voltage set to 4.7 kV. The second grid was held at ground potential. A venetian-blind secondary electron multiplier (SEM; EMI 9643, Electron Tubes Ltd., Ruislip, U.K.), equipped with a conversion dynode mounted 10 mm in front of the first dynode of the SEM, was used as ion detector. The post-acceleration potential applied to the conversion dynode was set to -20 kV for maximum detection sensitivity. SEM signals were amplified by a custom-built fast amplifier (impedance, $50\ \Omega$; amplification, ~ 5) and digitized and stored using the first channel of a digital oscilloscope (LeCroy 9345A, Chestnut Ridge, NY). The digitized data were transferred to a PC for subsequent data evaluation with laboratory-developed software programs.

Stress Wave Detection. Laser-induced photoacoustic stress waves were recorded with a piezoelectric ceramic disk sensor (FPM202, Marco, Hermsdorf, Germany; thickness, 5 mm; diameter, 10 mm). Both sides of the disk were metallized with $10\ \mu\text{m}$ CuNi for electrical contact. Samples were prepared directly on the CuNi surface. The sensor was integrated into a modified MALDI sample plate (Figure 2b), which was transferred into the ion source of the mass spectrometer and clamped into a bracket. For the simultaneous time-of-flight analysis of MALDI-generated ions, the whole target including both sides of the piezoelectric disk had to be held at the acceleration potential of 6 kV. Stress-induced piezoelectric signals were decoupled from high voltage (HV) via two $1\ \text{nF}$ HV capacitors, amplified by a custom-built differential amplifier (input impedance, $50\ \Omega$; amplification ~ 10 ; bandwidth, $\sim 130\ \text{MHz}$) and recorded using the second channel of the digital oscilloscope. Data analysis of the digitized signals was performed with PC-based laboratory-developed software.

Properties of the Piezoelectric Detection System. The signal response of the sensor and the following electronic circuit constitutes a crucial parameter in the experiments and has to be adapted carefully to the acoustic waveforms of interest. Two modes of operating a piezoelectric stress wave sensor can be distinguished, as discussed by Oraevsky and Karabutov.³⁰ The "more straightforward" way is to measure the idling voltage of the piezo at a high load resistance (e.g., $1\ \text{M}\Omega$). However, only in the static limit this open-circuit mode returns a voltage proportional to a constant pressure applied to the entire transducer.

The detection of stress waves with such a detection system is associated with certain crucial requirements because the idling voltage is, in this more general dynamic case, proportional to the path integral of the total stress transient inside the detector.³¹ Hence, the time resolution of an open-circuit system depends strongly on the thickness of the piezoelectric element. It can easily be estimated that time resolutions in the nanosecond range can be achieved only with detectors as thin as a few micrometers, which moreover have to be attached to an appropriate impedance-matched detector backing to avoid multiple acoustic reflections inside the piezo.

The detection system used in our present study has therefore been designed to be operated in an approximated short-circuit mode, avoiding the necessity of detector backings and micrometer-thin piezo elements. Because of the low input impedance of the employed differential amplifier of $50\ \Omega$, corresponding to the impedance of the connecting coaxial cables (see below), the piezo's discharge current is measured rather than its idling voltage. Because the idling voltage is proportional to the path

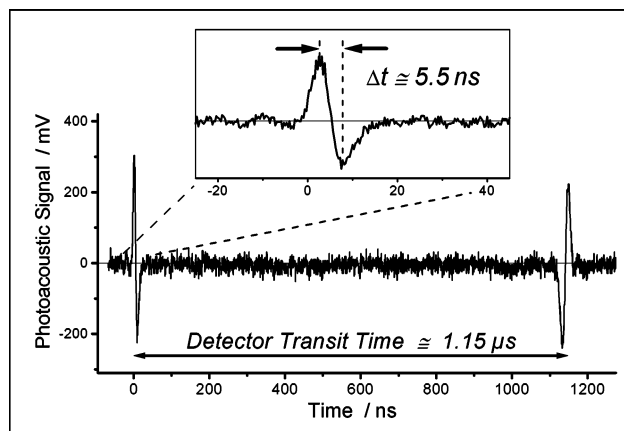


Figure 3. Photoacoustic test signal generated by the excitation of a thin dye layer from a felt-tip pen with an N_2 laser ($\lambda = 337\ \text{nm}$, $\tau_L = 4\ \text{ns}$) and recorded with the piezoelectric detection system. Note the two transient signals stemming from the stress wave passing through the detector's front and back surfaces, separated by a propagation time of $\sim 1.15\ \mu\text{s}$ through the piezoceramic. The distance between the compressive and tensile peak amplitude of $\sim 5.5\ \text{ns}$ reveals the time resolution of the detection system to be about $1.5\text{--}2\ \text{ns}$ (when compared to the expected $\sim 4\ \text{ns}$ determined by the excitation pulse duration).

integral of the stress transient inside the detector and the current is proportional to the time derivative of this voltage, a stress transient entering the detector induces a current signal proportional to its temporal profile, and a stress transient escaping the detector generates an equivalent signal with inverse polarity. Thus, a stress transient propagating through the entire detector will generate two signals of opposite polarity with a temporal delay corresponding to the detector's acoustic transit time. Unwanted interferences between these "front" and "back" surface signals can be avoided by choosing a sufficient transit time (i.e., an adequate detector thickness). The detector employed in our present study had a transit time of $\sim 1.15\ \mu\text{s}$ (Figure 3) during which stress transients can be measured without any disturbing self-interferences.

Contrary to open-circuit detection, for which the time resolution is given by the transducer thickness, the time resolution for short-circuit detection is given by the RC time constant of the transducer capacitance C and the amplifier load resistance R . In the detection system employed in our study, the short-circuit case was approximated by the utilization of an amplifier with a low input impedance of $50\ \Omega$. This value was chosen to match the wave resistance of the coaxial cables connecting transducer and amplifier for the avoidance of disturbing electromagnetic wave reflections inside the cables. With an overall capacitance (transducer and coupling capacitors) of $\sim 150\ \text{pF}$, the theoretical time resolution of the entire detection system can be estimated to be on the order of a few nanoseconds.

The functionality and, in particular, the time resolution of the piezoelectric detection system were evaluated in a test experiment with a short-pulsed N_2 laser (VSL-337ND, Laser Science Inc., Franklin, MA) of $\sim 4\ \text{ns}$ pulse duration and $337\ \text{nm}$ emission wavelength. A thin, UV-absorbing film of a dye from a felt-tip pen (Edding 3000, blue) was applied to the detector surface and irradiated at moderate fluences in the thermoelastic regime under ambient pressure. The resulting photoacoustic signal, as recorded by the detection system (including cables and differential amplifier), is shown in Figure 3, illustrating two relevant features. First, as expected for the short-circuit detection mode, the overall measured signal exhibits two bipolar transients stemming from the laser-generated stress

wave passing through the detector's front and back surface, with opposite polarities and a temporal delay corresponding to the detector transit time of $\sim 1.15 \mu\text{s}$. Moreover, the inset, which shows the front-surface signal of primary interest, displays the time resolution of the detection system. According to the theory, the peak stress amplitudes of the compressive and tensile partial waves should have a time separation approximately equal to the fwhm of the (Gaussian) excitation pulse. The experimentally determined separation is $\sim 5.5 \text{ ns}$, and by comparing this value to the laser pulse duration of $\sim 4 \text{ ns}$, we estimate the time resolution of the piezoelectric detection system to be about $1.5\text{--}2 \text{ ns}$.

We note that all measurements yielded relative values for the pressure as well as the amount of ejected material because an absolute calibration of the piezoelectric detection system was not performed (see also Discussion).

Excitation Lasers. Two different IR lasers were employed for the experiments. The first was an Er:YAG laser (Speser, Spektrum GmbH Berlin, Germany) of $2.94 \mu\text{m}$ emission wavelength and a pulse duration (fwhm) of $\sim 100 \text{ ns}$. The second laser was a wavelength-tunable optical parametric oscillator (OPO) (Mirage 3000B, Continuum, Santa Clara, CA; $\lambda = 1.4\text{--}4.0 \mu\text{m}$; $\tau_L = 6 \text{ ns}$). This laser system has been described in more detail previously.⁸ The OPO is pumped by the fundamental and second harmonic of a Nd:YAG laser (Surelite II-10, Continuum). In the present set of experiments, it was tuned to idler wavelengths of 2.94 (according to the Er:YAG laser emission wavelength), 3.05 , and $3.20 \mu\text{m}$. Residual 532 and 1064 nm pump laser radiation was blocked by the use of a germanium substrate placed at the Brewster angle into the laser beam line. (Germanium is fully opaque for wavelengths below $1.9 \mu\text{m}$.) Both lasers emit Gaussian-shaped temporal pulse profiles, as measured with a fast IR-sensitive HgCdTe detector (Radec Infrared-Detector R004-0, Boston Electronics Co., Brookline, MA; time resolution $< 2 \text{ ns}$). A fast pyroelectric detector (model 420, Eltec Instruments Daytona Beach, FL) was used to determine the instance of laser emission and to trigger the digital oscilloscope for measurements with the Er:YAG laser. For the experiments with the OPO, the oscilloscope was triggered directly by the Q-switch signal controlling the Pockels cell of the pump laser and preceding the actual output pulse by $\sim 130 \text{ ns}$.

Laser pulse energies were measured with a high-precision energy meter (RK320, Laser Precision Corp., NY) placed into the beam line. The maximum output energy of the Er:YAG laser was 4.5 mJ ; that of the OPO was about 1.5 mJ at all three employed wavelengths. The shot-to-shot variation of the laser pulse energy was about 8% for the Er:YAG and about 5% for the OPO laser (standard deviations).

At $2.94 \mu\text{m}$, laser fluences were adjusted by means of a dielectric attenuator with an optical transmission depending on the angle of incidence. For attenuation at the OPO wavelengths of 3.05 and $3.20 \mu\text{m}$, the dielectric filter was replaced by two counter-rotating germanium substrates, making use of the angular dependence of the reflection. Selected Schottglass filters were additionally placed into the beam line to extend the attenuation range.

Both laser beams were coupled into the ion source of the mass spectrometer via the same vacuum port and were focused onto the samples at an angle of incidence of 45° . Laser spot sizes were estimated by taking burn patterns on thermopaper (facsimile paper) attached to a standard target at carefully selected laser fluences, as described previously.⁸ Focal spot sizes

on the sample were approximately $110 \times 155 \mu\text{m}^2$ for the Er:YAG and $120 \times 170 \mu\text{m}^2$ for the OPO laser ($1/e^2$ definition).

Sample Preparation. Glycerol was purchased from Fluka, 2,5-dihydroxybenzoic acid (2,5-DHB) from Sigma Aldrich, and substance P from Bachem (Heidelberg, Germany). Glycerol samples were prepared by mixing glycerol with an aqueous analyte solution to produce an initial molar analyte-to-matrix ratio of $\sim 1:10^4$. A droplet of approximately $2\text{--}3 \mu\text{L}$ of the mixture was applied directly to the piezo surface with a pipet. Prior to transfer into the high vacuum of the mass spectrometer, most of the water content in the preparation was evaporated in the prevacuum ($\sim 10^{-2} \text{ mbar}$) for about 90 min . Typically, droplets of 1 mm in height and 2 mm in base diameter (after evaporating off the water) were prepared. The evaporation of glycerol in the high vacuum of the mass spectrometer led to continuous shrinkage of the droplet and increased the concentration of the analyte with time. Typically, a droplet would have evaporated completely within $3\text{--}4 \text{ h}$. However, the experimental runs were typically completed within 60 min , and neither the ion nor the ablation data were found to be notably affected by the change in droplet height (except for the acoustic signal transit time). Samples were irradiated at the apex of the drop at a repetition rate of 2 Hz . The time delay of 0.5 s between two exposures was sufficient for complete thermal and acoustic energy dissipation and the replenishment of the surface. Approximately 100 single PA signals were averaged for each laser fluence to enhance the signal-to-noise ratio and to level out laser energy fluctuations to a certain extent.

Substance P/2,5-DHB samples were prepared in the form of pressed "pellets" of about 1 mm thickness. To obtain samples of maximal homogeneity, 2,5-DHB and substance P were first cocrystallized from an aqueous solution with a molar analyte-to-matrix ratio of $1:5000$, similar to a normal dried-droplet preparation protocol. The obtained analyte-matrix crystals were then ground for several minutes in a ball mill (Perkin-Elmer, Norwalk, CT). The fine-ground powder was transferred to a hydraulic press (Perkin-Elmer; normally used to prepare KBr pellets for infrared spectroscopy). The fabricated pellets consisted of microscopically fine crystals of submicrometer size and were white and opaque in appearance, reminding of a ceramic material. Pellets of 13 mm diameter were fractured into four segments to fit onto the piezo surface, where they were attached with a thin film of vacuum grease, ensuring good acoustic contact between the pellet segment and the transducer.

Strong variations in the PA signals from the 2,5-DHB pellets were still observed if these were recorded from different pellet locations, probably due to reflections and scattering of stress waves at grain boundaries inside the pellets. Multiple exposures of selected single sample spots were not feasible because of the large amount of material removed per laser exposure, in particular at elevated fluences. To level out the influence of the inhomogeneities to some extent, approximately 100 single PA signals were therefore averaged for each laser fluence value, each taken from a previously non-irradiated spot on the pellet.

Signal Evaluation. Because of the slow but steady shrinkage of the glycerol preparations, the propagation time of PA signals in the droplet slightly decreased between subsequent measurements on the same sample. Hence, PA transients cannot be directly compared on an absolute time scale. For better comparability, photoacoustic signals will, therefore, be presented throughout this article as a function of the reduced time $\tau = t - z/c$, as defined above. In principle, the transformation from

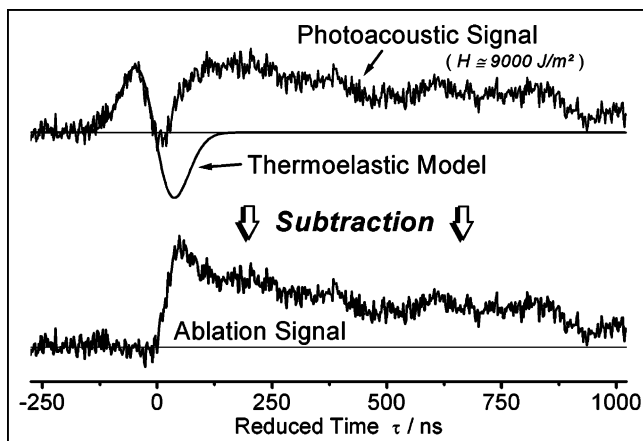


Figure 4. Illustration of the procedure for the extraction of the ablation-related signal component from an experimentally determined photoacoustic signal, in this case for the irradiation of glycerol with the Er:YAG laser ($\lambda = 2.94 \mu\text{m}$, $\tau_L = 100 \text{ ns}$). The amplitude of a thermoelastic model signal according to eq 5 was first fitted to an experimental thermoelastic signal (fluence, 2500 J m^{-2} ; Figure 5). The model signal was then multiplied by the ratio of the corresponding laser fluences ($9000/2500 = 3.6$), yielding the thermoelastic component of the displayed PA signal recorded at 9000 J m^{-2} . The difference of these two signals yields the ablation-related signal for the fluence of 9000 J m^{-2} .

the measured “real” time to the reduced time corresponds to a simple displacement on the time axis such that the crossover of a purely thermoelastic signal from compressive to tensile stress defines the origin on the τ scale (cf. eq 6). Such a thermoelastic “reference signal” was recorded for each set of experiments at a suitably low fluence. For the transformation of an ablation-influenced signal recorded at a higher fluence into the reduced time, the reference signal was scaled up in amplitude to the fluence of that signal, yielding essentially its thermoelastic component (consider the fluence proportionality of thermoelastic stresses), and their rising edges were aligned by means of a suitable time displacement. The crossover from compressive to tensile stress of the scaled-up reference signal then defines the $\tau = 0$ point. This procedure assumes that ablation is still negligible at the rising edge of the photoacoustic signal.

In some cases, the S/N ratios of the measured PA signals were rather low. Signals were therefore numerically processed by an FFT filter (cutoff frequency, 50 MHz) to diminish high-frequency electronic noise components prior to the alignment. PA signals generated with the Er:YAG laser were, however, still found to exhibit a very low S/N ratio after FFT filtering. Therefore, in this case, a thermoelastic model signal calculated according to eq 5 was used instead for the alignment and further signal processing.

The major advantage of transforming all measured signals into the reduced time domain is that, according to eq 10, the pure ablation-related signal components can now be extracted from the overall PA signals by a simple subtraction of the scaled-up thermoelastic reference signal. For clarity, this extraction procedure is illustrated in Figure 4.

Because this evaluation protocol turned out to be relatively time-consuming, a different approach was used where the temporal information was not of relevance (i.e., in the studies addressing the dependence of the overall amount of ejected material on the laser fluence). Here, photoacoustic signals were simply integrated numerically. According to eq 12, this yields the “ablation signal intensity” as a direct measure of the amount m_{total} of ablated material. Likewise, peak areas of the time-of-

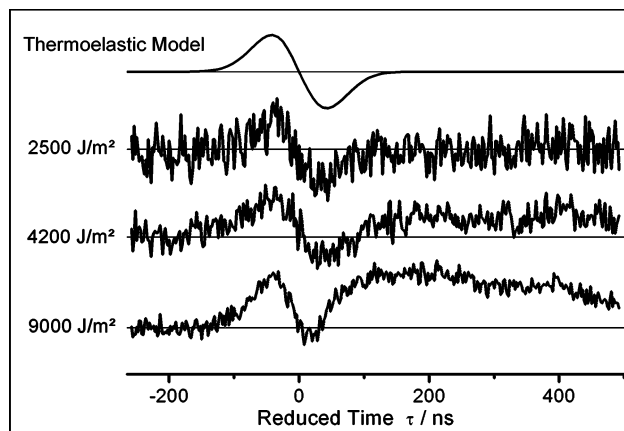


Figure 5. Photoacoustic signals generated in glycerol by irradiation with the Er:YAG laser ($\lambda = 2.94 \mu\text{m}$, $\tau_L = 100 \text{ ns}$) and different fluences as indicated on the left. A thermoelastic model signal, calculated according to eq 5, is also shown for comparison. Signals are represented in reduced time and have been multiplied by the reciprocal of the individual laser fluence. Successive elevation of the laser fluence results in a decrease of the relative tensile peak amplitude and a rise in the baseline after the thermoelastic signal.

flight spectra, recorded in parallel to the PA signals, serve as a measure of the number of generated ions. For both signal types, the individual “threshold fluence” is, throughout this article, defined as that fluence from which the signal-to-noise ratio of the averaged signals exceeds a value of 2.

Results

Glycerol: Time-Resolved Photoacoustic Signals. Figure 5 displays typical stress wave transients in glycerol generated by irradiation with the Er:YAG laser. Signals recorded at laser fluences of 2500 J m^{-2} (just below the MALDI ion threshold), 4200 J m^{-2} (typical MALDI fluence), and 9000 J m^{-2} (high side of typical MALDI fluence range) are plotted against the reduced time τ . For better comparability, signal amplitudes have been normalized to the individual laser fluence. A thermoelastic model signal, calculated according to eq 5 for the present material and irradiation parameters, is plotted in addition.

For fluences up to approximately 2700 J m^{-2} , photoacoustic signals are clearly dominated by the bipolar thermoelastic component. Also, apart from the relatively high noise level, the shape and width correspond exactly to those predicted by thermoelastic theory. In particular, the expected point symmetry (eq 6) between the compressive (plotted as positive signal in this and all other figures) and the tensile part of the stress wave signal is clearly observed. This experimental finding, therefore, justifies the data analysis by numerical integration outlined above.

With increasing laser fluence, the relative peak height of the leading compressive partial wave remains essentially unaltered (in the chosen fluence-scaled form of presentation). In contrast, the amplitude of the tensile part of the signal decreases systematically with fluence. Moreover, an additional compressive stress signal persists for long times after the thermoelastic signal. Both effects increase with laser fluence and can be directly accounted for by the superposition of a purely compressive ablation-related signal component. Material ejection hence exceeds the time of the thermoelastic signal considerably and lasts (measurably) for longer than a microsecond.

Photoacoustic signals generated in glycerol by the OPO are displayed in Figure 6 for the three excitation wavelengths of 2.94, 3.05, and $3.20 \mu\text{m}$ and a set of selected laser fluences.

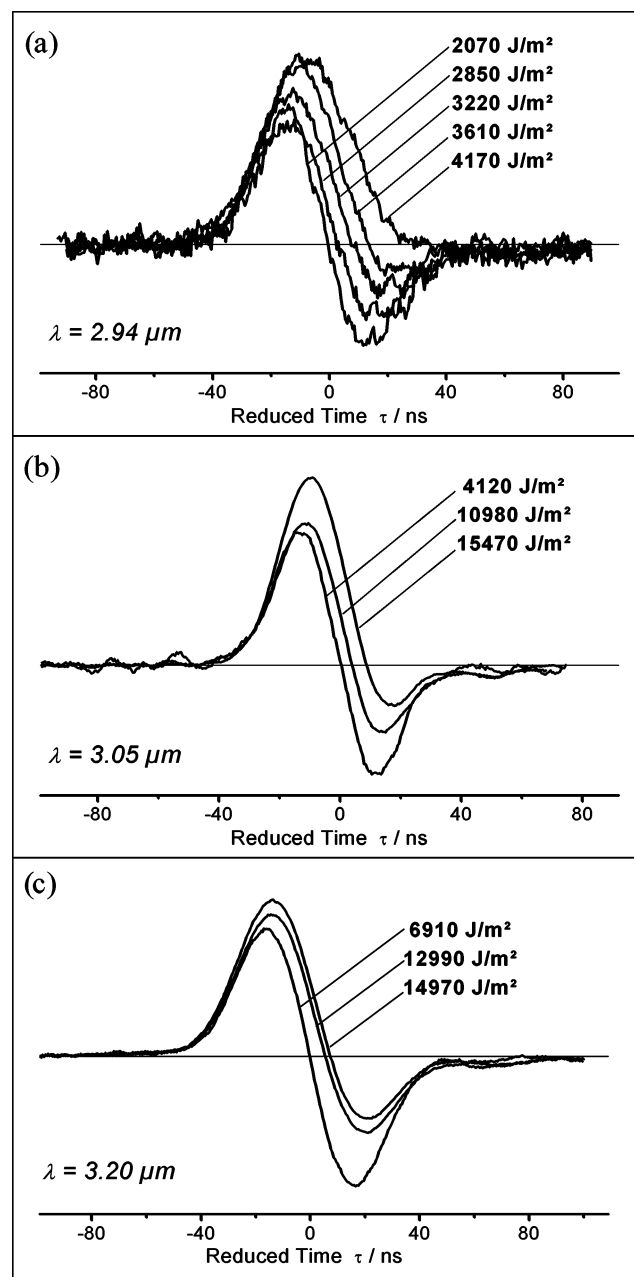


Figure 6. Photoacoustic transients generated in glycerol by irradiation with the OPO laser ($\tau_L = 6$ ns) for wavelengths of (a) 2.94, (b) 3.05, and (c) 3.20 μm , and different laser fluences. Signals are represented in reduced time and have been multiplied by the reciprocal of the individual laser fluence. For low fluences, essentially thermoelastic signals are recorded. Successive elevation of the fluence results in an increasing relative intensity of the compressive peak amplitude and a decreasing tensile amplitude for all three wavelengths. The baseline after the thermoelastic component remains unaffected in the investigated fluence range.

Again, signals have been normalized to the laser fluence. Compared to excitation with the Er:YAG laser, the dissipation of stress from the excitation volume during the laser pulse duration is significantly reduced. Consequently, S/N ratios of the PA signals are substantially higher for comparable fluence values. Likewise, as expected, S/N ratios also increase inversely with the optical absorption coefficient ($\alpha \sim 130 \text{ mm}^{-1}$ at 3.20 μm compared to $\sim 280 \text{ mm}^{-1}$ at 3.05 μm and $\sim 650 \text{ mm}^{-1}$ at 2.94 μm)⁸ because of enhanced stress confinement conditions.

For the data points recorded at the lowest fluences displayed in Figure 6, photoacoustic signals are again essentially thermo-

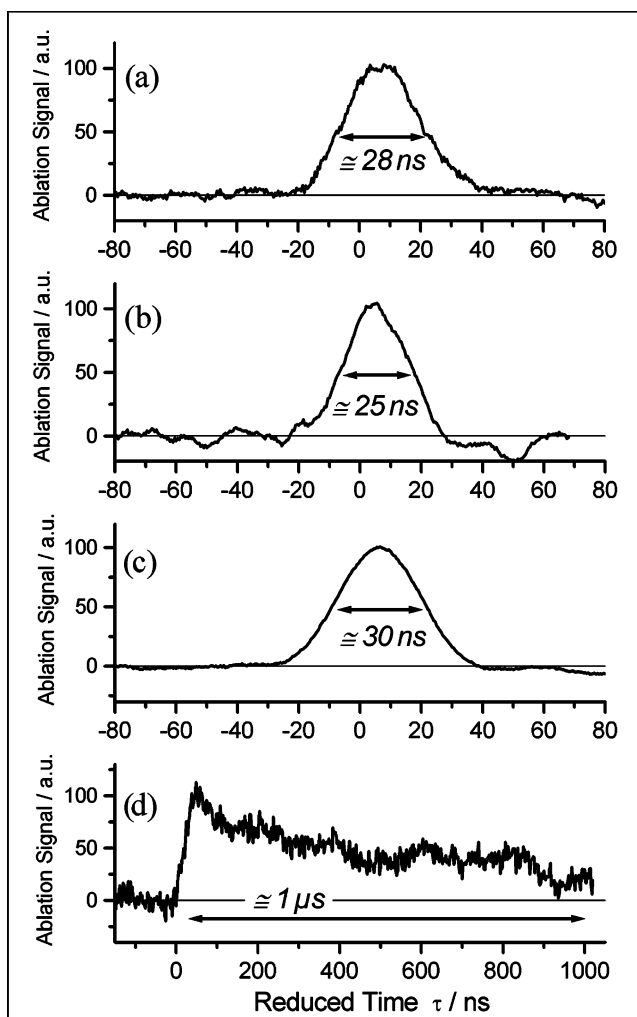


Figure 7. Representative ablation rate signals as extracted from the measured overall photoacoustic signals. (a) OPO; laser pulse duration, 6 ns; wavelength, 2.94 μm ; fluence, 4170 J m⁻². (b) OPO; wavelength, 3.05 μm ; fluence, 10 980 J m⁻². (c) OPO; wavelength, 3.20 μm ; fluence, 12 900 J m⁻². (d) Er:YAG laser; pulse duration, 100 ns; wavelength, 2.94 μm ; fluence, 9000 J m⁻². Signals are represented in reduced time and normalized to an arbitrary amplitude of 100. For all three OPO wavelengths, the time evolution is near-Gaussian with a fwhm of ca. 25–30 ns. In contrast, the Er:YAG ablation signal shows an approximately exponential decay characteristic with a time constant on the order of 1 μs .

elastic. As for the Er:YAG laser, the elevation of laser fluences gives rise to a reduction in the relative tensile amplitude because of material ejection. However, for excitation with the OPO, the scaled compressive amplitude also increases with fluence to some extent, indicating that in this case significant material ejection takes place already during the compressive part of the thermoelastic stress wave. Moreover, a persistence of compressive stress after the thermoelastic signal is not observed (i.e., ablation seems to be temporally rather well confined for the excitation with the OPO).

Glycerol: Extraction of the Time-Resolved Ablation Rates. Substantial differences in the processes of material ejection induced by the 6 and the 100 ns laser pulses become particularly evident if the pure ablation rate signals are extracted from the overall PA signals by subtracting the thermoelastic signal component, as outlined in the Experimental Section.

Representative ablation rate signals are displayed in Figure 7a–c for the three employed OPO wavelengths and in Figure 7d for excitation with the Er:YAG laser. For excitation with

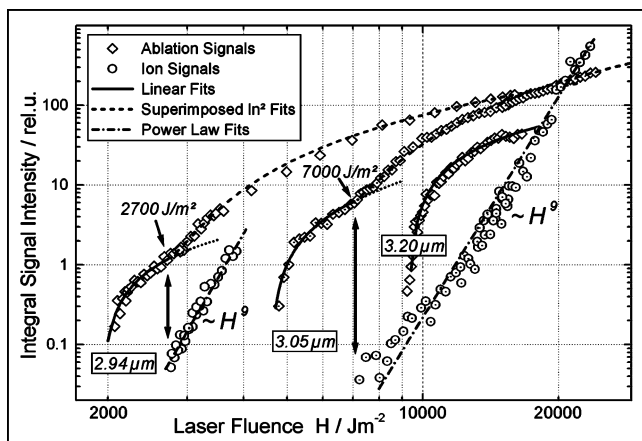


Figure 8. Integral ablation and ion signal intensities as determined from the measured ion (quasimolecular ions of substance P) and photoacoustic signals by numerical signal integration for the irradiation of a glycerol preparation with the OPO (pulse duration, 6 ns) at 2.94, 3.05, and 3.20 μm . For the 3.20 μm wavelength, the ion threshold fluence of approximately 26 kJ m^{-2} was not attainable in this experiment. Solid and dashed lines through the ablation data are best fits to model functions outlined in the discussion section. The dot-dashed lines through the ion data are best fits to a power function. The apparent kinks in the ablation curves, observed at a fluence of $\sim 2700 \text{ J m}^{-2}$ for $\lambda = 2.94 \mu\text{m}$ and $\sim 7000 \text{ J m}^{-2}$ for $\lambda = 3.05 \mu\text{m}$, indicate a change in the ejection mechanism. Both fluences correlate, moreover, with the corresponding threshold fluences for ion detection.

the 6 ns OPO pulses, the time evolution of the ablation rate signals is essentially the same for all three wavelengths. Signals are approximately Gaussian in shape and exhibit a fwhm of 25–30 ns. Ablation sets in at a reduced time below zero.

In the case of excitation with the 100 ns Er:YAG laser pulses, ablation sets in at a reduced time of about zero. The maximum ablation rate is reached at about 50 ns, followed by an approximately exponential decay with a characteristic time constant of about 1 μs .

For both lasers, only a minor dependence of the time evolution of the ablation signal on the laser fluence, visible as a slight broadening of the signals with increasing fluence on the order of nanoseconds, was notable in the data. The long-lasting exponential decay of the Er:YAG data was recorded over the entire investigated fluence range. Also, the quasi-Gaussian signal shapes were retained at all OPO wavelength/fluence combinations.

Glycerol: Increases in Integral Ablation and Ion Signals with Laser Fluence. The integral ablation signal intensities, corresponding to the overall amount of ablated material (eq 12), are displayed as a function of laser fluence in Figure 8 for excitation with the OPO and in Figure 9 for that with the Er:YAG. The Figures also contain the intensities of the in-parallel recorded MALDI ion signals of the substance P analyte, representing the number of detected ions. At an OPO wavelength of 3.20 μm , the maximum available laser fluence of $\sim 15 \text{ kJ m}^{-2}$ was not sufficient to generate any ion signals. Previous studies by Menzel et al. had determined the ion threshold at this wavelength to be about 26 kJ m^{-2} for comparable irradiation conditions.⁸ Below the (detectable) onset of material ejection, purely thermoelastic signals were recorded for all wavelength/pulse duration combinations down to fluences of about 2000 J m^{-2} . As expected, their peak amplitudes were found to rise strictly linearly with fluence.

The solid and dashed lines through the ablation data are best fits according to theoretical models (see discussion below). The dot-dashed lines through the ion signal data are best fits to a

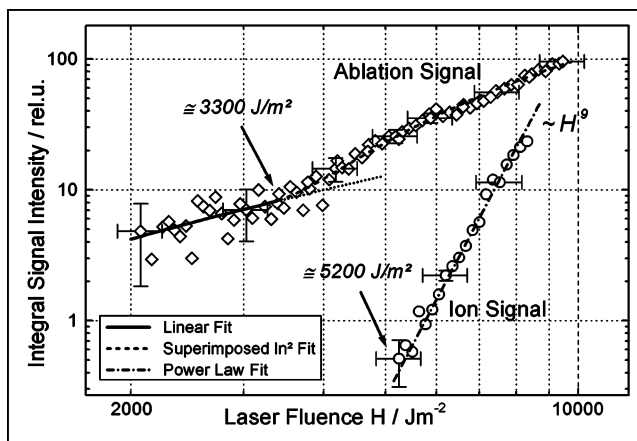


Figure 9. Integral ablation and ion-signal intensities as determined from the measured ion (quasimolecular ions of substance P) and photoacoustic signals by numerical signal integration for the irradiation of a glycerol preparation with the Er:YAG laser (pulse duration, 100 ns; wavelength, 2.94 μm). Solid and dashed lines through the ablation data are best fits to model functions outlined in the discussion section. The dot-dashed line through the ion data is a best fit to a power function. The arrow pointing to the ablation data indicates a possible change in the mechanisms, which is, however, less obvious than in the OPO data of Figure 8.

power law of the form $I_{\text{ion}} \propto H^m$, where I_{ion} is the ion signal intensity, H is the laser fluence, and m is an exponent corresponding to the slope in the double-logarithmic representation. For both ablation lasers, the ion data were fitted best with an m of ~ 9 , in good agreement with the results from a previous investigation in which the same Er:YAG laser was employed.³²

For both lasers and all wavelengths, substantial ablation takes place at fluences considerably below the MALDI ion detection threshold. The data do not allow to draw definite conclusions about the exact ablation threshold because the low-fluence signal limit could either be determined by a physical threshold for material ejection or by the limit in detection sensitivity.

2,5-DHB Pellets: Time-Resolved PA Signals. Major problems in all measurements with crystalline matrix preparations were poor signal reproducibility and generally relatively low S/N ratios of the PA signals. Therefore, only the OPO was used in these measurements. All attempts to use standard dried-droplet matrix preparations did not produce sufficiently reproducible results for any of the tested crystalline matrix compounds (2,5-DHB, succinic acid, thiourea). Not even the utilization of large, slowly grown crystals of these compounds³³ resulted in the necessary improvement. Instead, best results were obtained if samples were prepared in the form of pressed flat pellets as described in the Experimental Section. From the tested matrices, 2,5-DHB was found to yield the most reproducible data. Therefore, only this matrix has been studied in more detail.

Time-resolved PA signals from a 2,5-DHB pellet preparation are displayed in Figure 10 for laser fluences of 2660, 5440, and 9150 J m^{-2} . Again, PA signals have been “normalized” by multiplying them by the inverse of the individual laser fluence value. Up to a fluence of about 3000 J m^{-2} , essentially bipolar and symmetric thermoelastic signals are detected. At higher fluences, the relative peak amplitude of the tensile partial wave diminishes due to the onset of material ejection, while the scaled amplitude of the compressive partial wave increases strongly with fluence.

Two representative reconstructed ablation rate signals are shown in Figure 11 for laser fluences of 5440 and 9150 J m^{-2} . It should be noted that, because of the averaging procedure of

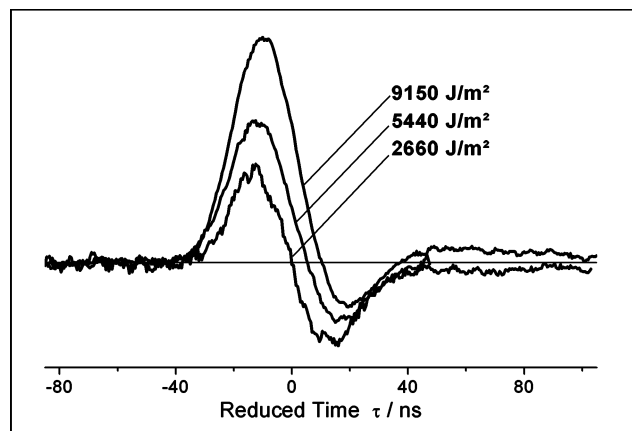


Figure 10. Photoacoustic signals from a 2,5-DHB pellet preparation irradiated with the OPO (laser pulse duration, 6 ns) at a wavelength of $2.94\ \mu\text{m}$ and different fluences. Each trace shows the average signal of approximately 100 single laser exposures at different spots on the pellet. The signals have been multiplied by the reciprocal of the individual laser fluence values. The low-fluence signal recorded at $2660\ \text{J m}^{-2}$ exhibits a purely thermoelastic characteristic. Elevation of the laser fluence results in an increase of the relative intensities of the compressive peak amplitude and a decrease of the scaled tensile amplitude.

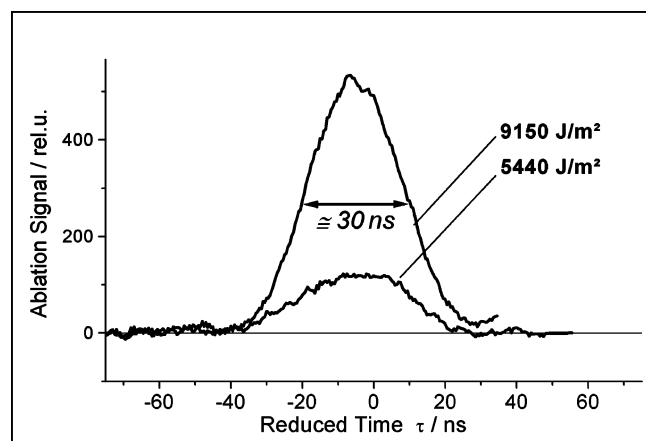


Figure 11. Ablation rate signals as extracted from the photoacoustic signals for the irradiation of a 2,5-DHB pellet preparation with the OPO (laser pulse duration, 6 ns; wavelength, $2.94\ \mu\text{m}$). Each trace shows the average signal of approximately 100 single laser exposures at different spots on the pellet. Except for the amplitude, the time evolution is essentially the same for both traces, showing a near-Gaussian characteristic with a fwhm of about 30 ns.

the raw PA signals, the ablation rate signals must also be considered to be “averaged”. Conclusions about the temporal evolution of individual ablation events can therefore be drawn only with great caution. Nevertheless, it is evident that material ejection from the 2,5-DHB pellets is temporally well confined for irradiation with the short OPO laser pulse. The negative values in the reduced time data moreover suggest that material ejection commences during the compressive part of the stress wave and even a little earlier than for glycerol.

2,5-DHB Pellets: Increase of Ablation and Ion Signals with Laser Fluence. The integral ablation and substance P ion signal intensities are plotted in Figure 12. Despite the rather poor reproducibility of the single-shot PA signals, the resulting set of averaged data points yields a surprisingly smooth curve. The MALDI ion detection threshold for desorption/ionization from this matrix is about $3000\ \text{J m}^{-2}$, in agreement with previously reported values for a comparable laser spot size.³²

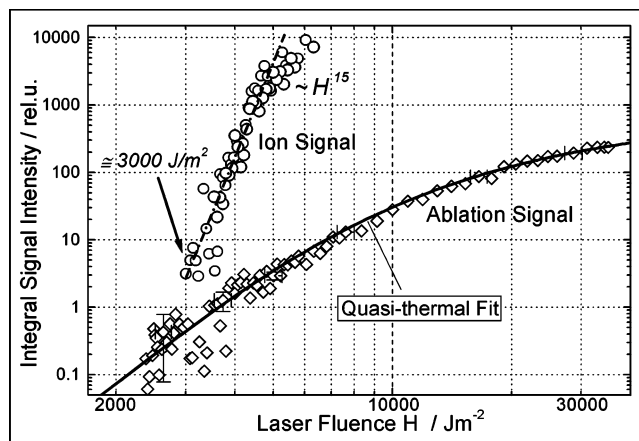


Figure 12. Integral ablation and ion signal intensities as determined from the measured ion (quasimolecular ions of substance P) and photoacoustic signals by numerical signal integration for the irradiation of a 2,5-DHB pellet preparation with the OPO (laser pulse duration, 6 ns; wavelength, $2.94\ \mu\text{m}$). The dot-dashed line through the ion data is the best fit to a power function; the solid line through the ablation data is a best fit according to a quasi-thermal desorption model (eq 16) with parameters of $T_0 = 293\ \text{K}$, $E_a = 0.45\ \text{eV}$, and $\eta = 0.14\ \text{K m}^2\ \text{J}^{-1}$ (see Discussion).

As for glycerol, the increase in the ion signal intensity with fluence is much steeper than that of the material ablation.

Discussion

Glycerol. Whereas the mathematical model of eq 5 provides an excellent description of the time course of experimental Er:YAG laser-generated thermoelastic stress wave signals, these are notably “stretched” for the OPO exposure at all three wavelengths: compressive and tensile peak amplitudes are about 25 ns apart (for a glycerol droplet height of $\sim 1\ \text{mm}$ as applied in these experiments; see low-fluence signals in Figure 6) whereas the model predicts a time separation on the order of the laser pulse duration (6 ns) only. Our test experiment with the UV laser proved that this broadening cannot be caused by an insufficient time resolution of the detection system (Figure 3). However, it can be partially explained by the three-dimensional propagation of a spherical stress wave within the sample induced by acoustic diffraction. Laser-induced spherical stress wave generation has been discussed in detail by Sigrist.³⁴ By adopting his mathematical treatment to the experimental conditions of our study, the transition from a plane to a spherical stress wave (i.e., transition from near- to far-field) can be calculated to take place at a depth in the sample of approximately $230\ \mu\text{m}$. Hence, for glycerol droplets of larger height, spherical waves are detected by the planar detector. Note that the curvature of the glycerol droplet itself is negligible across the irradiated spot. Care was also taken to irradiate exactly the apex of the glycerol droplet. Following the theory of Sigrist, the formation of a spherical stress wave, in combination with the planar detector surface, can indeed stretch the thermoelastic signal of 6 ns peak separation to approximately the experimentally observed 25 ns separation for a droplet height of $\sim 1\ \text{mm}$. Similar calculations reveal that signal broadening due to spherical wave propagation is negligible in case of the 100 ns Er:YAG laser excitation.

To further elucidate the relevance of spherical wave propagation, OPO-generated photoacoustic signals were recorded from glycerol droplets of different heights ranging from 0.05 to 1.1 mm for a constant laser fluence of $2100\ \text{J m}^{-2}$ in the thermoelastic range. A reduction in signal width and in the

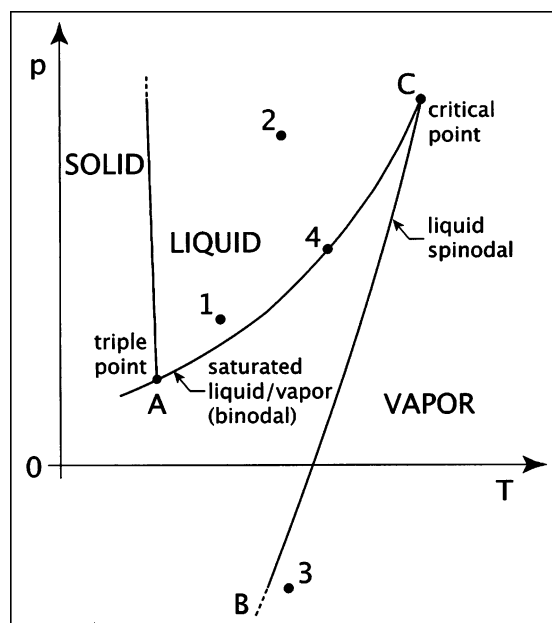


Figure 13. Path taken through the p vs T projection of the thermodynamic phase diagram for a temperature rise above the boiling temperature under stress confinement conditions (according to the irradiation of glycerol with the 6 ns OPO pulse). The 1 \rightarrow 2 transition corresponds to the heating phase that is coupled with the generation of compressive stress. The 2 \rightarrow 3 transition corresponds to the passage of the tensile stress wave that leads to a crossing of the spinodal limit, resulting in explosive phase separation. Point 4 represents the state of the system after phase explosion with two separated phases. Reprinted with permission from ref 26; copyright ACS, 2003.

temporal separation of the compressive and tensile peak amplitudes was indeed observed when the droplet height was reduced. However, even for the smallest height of 50 μm (for which the approximation of a plane wave clearly holds), the peak amplitude separation did not fall below 15 ns. Compared to the thermoelastic model, the experimental signals were therefore still stretched by a factor of more than 2. The reasons for this remaining signal broadening could not finally be clarified in the scope of this study. A likely reason is a frequency-dependent acoustic absorption and/or dispersion of the acoustic wave inside the glycerol medium. Material data necessary for further elucidation of these latter effects were, unfortunately, not available for glycerol.

The remarkably different time evolution of the glycerol ablation rate signals for the two laser pulse durations of 6 and 100 ns can be directly associated with the different extent of stress confinement. With a laser penetration depth α^{-1} of about 1.5 μm at the excitation wavelength of 2.94 μm ⁸ and a speed of sound in glycerol of $\sim 1900 \text{ m s}^{-1}$, the characteristic time for acoustic energy dissipation, $\tau_{\text{ac}} = \alpha^{-1}c^{-1}$, is on the order of $\sim 1 \text{ ns}$. Hence, whereas the build-up of high bipolar thermoelastic stresses is rather negligible for the 100 ns Er:YAG excitation pulse,³⁵ it can contribute decisively to the overall process for the 6 ns OPO pulse. For instance, for a typical fluence of 5000 J m^{-2} and a wavelength of 2.94 μm , peak amplitudes of the thermoelastic stress wave are calculated according to eq 5 to be about 50 MPa for the 6 ns pulse, as compared to only 250 kPa for the 100 ns Er:YAG pulse.

Following the argumentation by aus der Wiesche et al.³⁶ and Vogel and Venugopalan,²⁶ the propagation of such a strong bipolar stress wave through a (super-)heated liquid volume can promote very rapid homogeneous nucleation over a large spatial scale and eventually lead to instantaneous “spinodal decomposition” (i.e., a phase explosion of entire excited volume elements

on the time scale of the laser pulse duration). The basic concept of this proposed mechanism can be read off of a schematic pT projection of the phase diagram (Figure 13): Energy deposition by the laser leads to both rapid heating and pressure build-up inside the excitation volume. In the pT diagram, this corresponds to a transition from initial state 1 to state 2. Upon propagation of the rarefaction wave through the excited volume, a transition from state 2 to state 3 takes place. In the regime of stress confinement (OPO), state 3 can easily be in the unstable region beyond the spinodal (as indicated in the Figure).

Moreover, because the achieved temperature in surface volume elements can be estimated to be about several hundred Kelvin, even point 2 in the pT diagram, representing the end of the heating pulse, might already be close to the critical point of glycerol (765 K, 4.3 MPa³⁷), and spinodal decomposition may therefore commence already during the compressive thermoelastic part wave.³⁸ The onset of the ablation rate signals at negative reduced times in Figure 7 would reflect this fact.

In contrast, for the Er:YAG laser with only a moderate increase in pressure, state 2 is likely to be located in the metastable region between the binodal and the spinodal and not to be shifted very much by the only very minor pressure amplitudes. Sizable homogeneous nucleation is therefore not induced. Instead, the temperature increase goes along with heterogeneous nucleation and bubble diffusion, the latter process setting the microsecond time scale for material ejection.

We note that thermal confinement conditions are fulfilled for both laser pulse durations. For the given irradiation geometry, the characteristic time τ_{th} for heat dissipation in glycerol can be estimated according to

$$\tau_{\text{th}} = \frac{\rho C_p \delta^2}{4\lambda_{\text{th}}} \quad (13)$$

where ρ is the density ($1.26 \times 10^3 \text{ kg m}^{-3}$), C_p is the specific heat at constant pressure ($2.36 \times 10^3 \text{ J kg}^{-1} \text{ K}^{-1}$; $p = 1 \text{ bar}$), and λ_{th} is the thermal conductivity ($0.3 \text{ W m}^{-1} \text{ K}^{-1}$) of glycerol at ambient pressure and temperature. Using these equilibrium values, eq 13 results in a value of $\tau_{\text{th}} \approx 6 \mu\text{s}$, which is considerably longer than both laser pulses.

Although we did not perform an absolute calibration of the signal response of our piezoelectric detector, a rough estimate for the removed material can be obtained by applying photoacoustic theory. This holds in particular for excitation with the Er:YAG laser, for which the agreement between theoretical and experimental wave forms is excellent. For example, for a fluence of 9000 J m^{-2} , the theoretical peak amplitude of the thermoelastic stress wave component can be calculated from eq 5 to be $\sim 450 \text{ kPa}$. Using this value as a “calibration” for the overall photoacoustic signal measured at that fluence (shown in Figure 4), an absolute value for the time integral of the ablation-related signal (lower trace in Figure 4) of $\sim 0.25 \text{ Pa s}$ is derived, corresponding to the forward momentum of the ablated mass per ejection area (eq 12). Dividing this quantity by an estimated mean ejection velocity \bar{v} of 500 m s^{-1} ⁹ and the mass density ρ of glycerol ($1.26 \times 10^3 \text{ kg m}^{-3}$), one obtains an averaged ejection depth of $\sim 0.4 \mu\text{m}$ corresponding to $\sim 7 \text{ pg}$ of removed material per laser pulse.

With absorption values α of $\sim 650 \text{ mm}^{-1}$ for a wavelength of 2.94 μm , $\sim 280 \text{ mm}^{-1}$ for 3.05 μm , and $\sim 130 \text{ mm}^{-1}$ for 3.20 μm ,⁸ almost identical volumetric energy densities $\epsilon = \alpha H$ at the glycerol surface of $\sim (1.2\text{--}1.3) \times 10^9 \text{ J m}^{-3}$ (corresponding to 88–95 kJ mol^{-1}) are calculated for the ablation signal “thresholds” of ~ 2000 , ~ 4700 , and $\sim 9000 \text{ J m}^{-2}$, respectively.

The latent heat of vaporization of glycerol is $\sim 73 \text{ kJ mol}^{-1}$,³⁹ and the sensible heat to warm glycerol from ambient to boiling temperature (563 K at $p = 1 \text{ bar}$) is 59 kJ mol^{-1} . Naturally, the latter value can serve only as a crude estimate because the low background pressure in the mass spectrometer will lower the boiling temperature for surface evaporation considerably,⁴⁰ as will the propagation of the bipolar stress wave through the excited volume and bubble formation within that volume. A comparison with the deposited volumetric energies nevertheless indicates that vaporization of glycerol can readily be achieved.

The apparent kinks in the ablation versus fluence curves, observed at 2700 J m^{-2} for the $2.94 \text{ }\mu\text{m}$ OPO wavelength, 7000 J m^{-2} for the $3.05 \text{ }\mu\text{m}$ OPO wavelength, and 3300 J m^{-2} for the Er:YAG laser (Figures 8 and 9), indicate two different regimes for material ejection at low and high fluences.⁴¹ For the $3.20 \text{ }\mu\text{m}$ wavelength, the available maximum laser energy was likely not sufficient to access the second regime.

In the low-fluence regime, ablation increases strictly linearly with laser fluence for all tested laser wavelength/pulse duration combinations (solid lines in Figures 9 and 10):

$$I_{\text{Abl,I}}(H) \propto \alpha^{-1}(H - H_I(\lambda)), \quad H > H_I \quad (14)$$

$I_{\text{Abl,I}}$ is the integral ablation signal, and H_I is the experimental ablation threshold.

In the high-fluence regime, a “blow-off model”²⁶ superimposed on the linear relation of eq 14 was found to describe the experimental data in excellent agreement for both lasers (dashed lines in Figures 8 and 9):

$$I_{\text{Abl,II}}(H) \propto I_{\text{Abl,I}}(H) + \left[\ln\left(\frac{H}{H_{\text{II}}}\right) \right]^2, \quad H > H_{\text{II}} \quad (15)$$

$I_{\text{Abl,II}}$ is the integral ablation signal above a transition threshold H_{II} . The second term of the equation describes the ejection of entire volume elements down to a depth of z_{cr} for which the deposited energy density exceeds a critical value ϵ_{cr} , set by the material properties. Note that the logarithmic function is squared because of the spatial Gaussian intensity profile of the excitation laser beam;⁴² it would be a linear logarithm for a rectangular intensity profile. That eq 15 also contains the linear term in eq 14 can be attributed to the Gaussian beam profile as well: the critical energy density for collective material removal is reached only in the central part of the laser spot, but material ejection according to process I continues to take place from the peripheral areas and possibly also from volume elements below z_{cr} . However, compared to the strong increase in the logarithmic part of the equation, the contribution of the linear term is minor, and it rather defines the vertical offset at H_{II} . Attempts to fit the integral ablation intensities with other model functions (e.g., with a quasi-thermal model, eq 16) did not result in any satisfying agreement with the experimental data.

Figure 8 shows that the onset of the second ablation regime at H_{II} correlates with the onset of ion detection for the two OPO wavelengths of 2.94 and $3.05 \text{ }\mu\text{m}$. For the Er:YAG laser, such a correlation is not evident (Figure 9). It is not yet known whether this correlation does indeed reflect a unique feature of the ionization mechanism for the short-pulsed excitation with the OPO. Mass spectrometric evidence for differences in the ionization pathways for IR-MALDI with glycerol and the two laser pulse durations was, however, also found in recent work by Menzel et al.,⁴³ in that case, the evidence was visible in a slightly modified distribution of analyte charge states and oligomerization.

2,5-DHB Pellets. Compared to glycerol, 2,5-DHB material properties differ in relevant aspects: The sample constitutes a rather inhomogeneous microcrystalline entity with a large number of grain boundaries within the excitation volume. Also, the optical absorption coefficient at $2.94 \text{ }\mu\text{m}$ is about a factor of 4–9 smaller than that of glycerol.³²

In fact, the dependence of the ablation signal intensity on fluence follows entirely different routes for the two test matrices. For 2,5-DHB, the best fit to the experimental data (solid line in Figure 12) is obtained with a quasi-thermal vaporization model:¹⁷

$$I_{\text{Abl}}(H) = P \cdot e^{-E_a/k_B(T_0 + \eta H)} \quad (16)$$

P is a (possibly fluence-dependent) preexponential factor, E_a is the activation energy for the process, k_B Boltzmann's constant, and $\eta = \Delta T/H$ is a conversion factor describing the temperature increase induced by the absorption of the laser energy. The solid line in Figure 12 is a best fit to the data with $E_a = 0.45 \text{ eV}$ (according to 43.4 kJ mol^{-1}) and $\eta = 0.14 \text{ K m}^2 \text{ J}^{-1}$. Equation 16 fits the entire investigated fluence range (i.e., a “kink” indicating a transition between different regimes is not notable in the 2,5-DHB data).

To a first (equilibrium) approximation (neglecting possible reflection losses, temperature-induced changes in the parameters, and phase transitions), η would be given by $\eta = \alpha(\gamma\rho C_V)^{-1}$, where γ accounts for (loss) processes other than thermal heating. Assuming γ to be equal to 1 and using tabulated values for 2,5-DHB of $\rho = 1.57 \times 10^3 \text{ kg m}^{-3}$, $C_V = 1.045 \text{ kJ kg}^{-1} \text{ K}^{-1}$, and $\alpha \sim 100 \text{ mm}^{-1}$ for an excitation wavelength of $2.94 \text{ }\mu\text{m}$,³² η can be estimated to be $\sim 7 \times 10^{-2} \text{ K m}^2 \text{ J}^{-1}$. The value of $0.14 \text{ K m}^2 \text{ J}^{-1}$ derived from the best fit is close to this theoretical estimate.

As for glycerol, integral ion signals rise much more strongly with fluence than the material ejection, demonstrating that the ionization efficiency is highly fluence-dependent. Compared to our previous investigation,³² the increase in the analyte ion signal with laser fluence is significantly higher: the power law fit yields an exponent m of ~ 15 (Figure 12), whereas in ref 32 an m of only 4–5 was determined for the 2,5-DHB matrix. These differences are likely caused by the utilization of a Gaussian beam profile in the present study, in contrast to the flat-top, homogeneous beam profile used in ref 32. Test experiments with different types of preparation showed that the larger slope is not caused by the sample preparation. However, additional studies are clearly necessary to further address this interesting observation. It should also be pointed out that a beam-profile-dependent change in the ion signal increase was not observed for glycerol. Here, $m \sim 9$ was determined for both beam profiles.

Conclusions

The piezoelectric detection scheme described in this article allowed us to record the rate of material ejection in IR-MALDI with a temporal resolution of a few nanoseconds. Furthermore, the proposed data evaluation protocol permitted the straightforward extraction of the ablation-related signal component from the overall photoacoustic signal. Moreover, the procedure allowed us to determine the relative amounts of ablated material by simple signal integration (e.g., as a function of laser fluence). These approaches are naturally not restricted to the MALDI case. However, the integration of the piezoelectric detector into a mass spectrometric system allowed the simultaneous sensitive detection of laser-generated ions and hence a direct comparison between ablation and ionization data.

A comparison between the processed and the raw data shows that this evaluation scheme has many advantages if details of the processes shall be revealed. For example, in previous photoacoustic studies (e.g. by Cross et al.²³ and Venugopalan et al.^{24,25} on laser ablation from tissue), only the peak compressive stresses of the overall photoacoustic signals were evaluated. A stepwise increase in the peak stress amplitude was observed in both studies and associated with the onset of explosive ablation. However, material ejection below the apparent ablation threshold could eventually not be revealed with that evaluation protocol, nor could the exact time course of material ejection.

Acknowledgment. We thank Arne Leisner for the development of sophisticated data evaluation software and Vasanth Venugopalan, Leonid V. Zhigilei, and Barbara Garrison for fruitful discussions. A.R. is grateful to the University of Münster for a Ph.D. grant. L.M.K. thanks the Alexander-Von-Humboldt Stiftung for a fellowship. This work has been carried out in partial fulfillment of the requirements for the Ph.D. in Experimental Physics by A.R. at the University of Münster.

References and Notes

- (1) Karas, M.; Bachmann, D.; Bahr, U.; Hillenkamp, F. *Int. J. Mass Spectrom. Ion Processes* **1987**, 78, 53.
- (2) Karas, M.; Hillenkamp, F. *Anal. Chem.* **1988**, 60, 2299.
- (3) Beavis, R. C.; Chait, B. T. *Rapid Commun. Mass Spectrom.* **1989**, 3, 233.
- (4) Overberg, A.; Karas, M.; Bahr, U.; Kaufmann, R.; Hillenkamp, F. *Rapid Commun. Mass Spectrom.* **1990**, 4, 293.
- (5) Overberg, A.; Karas, M.; Hillenkamp, F. *Rapid Commun. Mass Spectrom.* **1991**, 5, 128.
- (6) Cramer, R.; Haglund, R. F.; Hillenkamp, F. *Int. J. Mass Spectrom. Ion Processes* **1997**, 169/170, 51.
- (7) Caldwell, K. L.; McGarity, D. R.; Murray, K. K. *J. Mass Spectrom.* **1997**, 32, 1374.
- (8) Menzel, C.; Dreisewerd, K.; Berkenkamp, S.; Hillenkamp, F. *Int. J. Mass Spectrom.* **2001**, 207, 73.
- (9) Dreisewerd, K.; Berkenkamp, S.; Leisner, A.; Rohlfing, A.; Menzel, C. *Int. J. Mass Spectrom.* **2003**, 226, 189.
- (10) Berkenkamp, S.; Kirpekar, F.; Hillenkamp, F. *Science* **1998**, 281, 260.
- (11) Cramer, R.; Richter, W. H.; Stimpson, E.; Burlingame, A. L. *Anal. Chem.* **1998**, 70, 4939.
- (12) Dreisewerd, K. *Chem. Rev.* **2003**, 103, 295.
- (13) Poretzky, A. A.; Geohegan, D. B. *Chem. Phys. Lett.* **1998**, 286, 425.
- (14) Niu, S. F.; Zhang, W. Z.; Chait, B. T. *J. Am. Soc. Mass Spectrom.* **1998**, 9, 1.
- (15) Knochenmuss, R.; Stortelder, A.; Breuker, K.; Zenobi, R. *J. Mass Spectrom.* **2000**, 35, 1237.
- (16) Huth-Fehre, T.; Becker, C. H. *Rapid Commun. Mass Spectrom.* **1991**, 5, 378.
- (17) Dreisewerd, K.; Schürenberg, M.; Karas, M.; Hillenkamp, F. *Int. J. Mass Spectrom. Ion Processes* **1995**, 141, 127.
- (18) Mowry, C. D.; Johnston, M. V. *Rapid Commun. Mass Spectrom.* **1993**, 7, 569.
- (19) Mowry, C. D.; Johnston, M. V. *J. Phys. Chem.* **1994**, 98, 1904.
- (20) Dreisewerd, K.; Schürenberg, M.; Karas, M.; Hillenkamp, F. *Int. J. Mass Spectrom. Ion Processes* **1996**, 154, 171.
- (21) Dyer, P. E.; Srinivasan, R. *Appl. Phys. Lett.* **1986**, 48, 445.
- (22) Paltauf, G.; Dyer, P. E. *Chem. Rev.* **2003**, 103, 487.
- (23) Cross, F. W.; Al-Dhahir, R. K.; Dyer, P. E. *J. Appl. Phys.* **1988**, 64, 2194.
- (24) Venugopalan, V.; Nishioka, N. S.; Mikić, B. B. *Biophys. J.* **1996**, 69, 1259.
- (25) Venugopalan, V.; Nishioka, N. S.; Mikić, B. B. *Biophys. J.* **1996**, 70, 2981.
- (26) Vogel, A.; Venugopalan, V. *Chem. Rev.* **2003**, 103, 577.
- (27) Westmacott, G.; Ens, W.; Hillenkamp, F.; Dreisewerd, K.; Schürenberg, M. *Int. J. Mass Spectrom.* **2002**, 221, 67.
- (28) Gournay, L. S. *J. Acoust. Soc. Am.* **1966**, 40, 1322.
- (29) Berkenkamp, S.; Menzel, C.; Hillenkamp, F.; Dreisewerd, K. *J. Am. Soc. Mass Spectrom.* **2002**, 13, 209.
- (30) Oraevsky, A. A.; Karabutov, A. *Proc. SPIE* **2000**, 3916, 228.
- (31) Krautkrämer, J.; Krautkrämer, H. *Ultrasonic Testing of Materials*; Springer-Verlag: Berlin, 1990; Chapter 7.
- (32) Feldhaus, D.; Menzel, C.; Berkenkamp, S.; Hillenkamp, F.; Dreisewerd, K. *J. Mass Spectrom.* **2000**, 35, 1320.
- (33) Kampmeier, J.; Dreisewerd, K.; Schürenberg, M.; Strupat, K. *Int. J. Mass Spectrom. Ion Processes* **1997**, 169/170, 31.
- (34) Sigrist, M. W. *J. Appl. Phys.* **1986**, 60, R83.
- (35) Dingus, R. S.; Scammon, R. J. *SPIE* **1991**, 1427, 45.
- (36) Aus der Wiesche, S.; Rember, C.; Hofer, E. P. *Heat Mass Transfer* **1999**, 35, 143.
- (37) <http://physchem.ox.ac.uk/MSDS/GL/glycerol.html>.
- (38) Miotello, A.; Kelly, R. *Appl. Phys. A* **1999**, 69, S67.
- (39) *CRC Handbook of Chemistry and Physics*, 67th ed.; Weast, R. C., Ed.; CRC Press: Boca Raton, FL, 1987.
- (40) Stull, D. R. *Ind. Eng. Chem.* **1947**, 39, 517.
- (41) Zhigilei, L. V.; Garrison, B. J. *J. Appl. Phys.* **2000**, 88, 1281.
- (42) Johnson, R. E. *Int. J. Mass Spectrom. Ion Processes* **1994**, 139, 25.
- (43) Menzel, C.; Dreisewerd, K.; Berkenkamp, S.; Hillenkamp, F. *J. Am. Soc. Mass Spectrom.* **2002**, 13, 975.